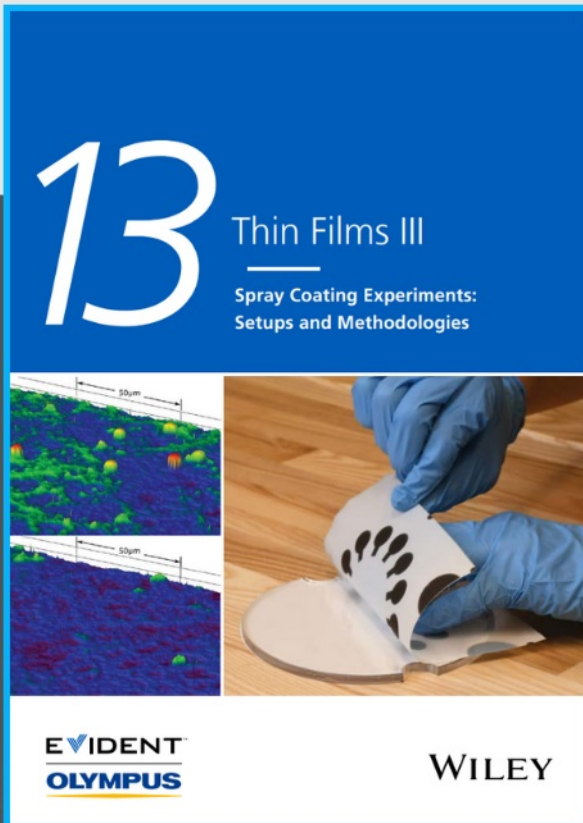




Spray Coating Experiments: Setups and Methodologies



**The latest eBook from
Advanced Optical Metrology.
Download for free.**

Spray Coating Experiments: Setups and Methodologies, is the third in our Thin Films eBook series. This publication provides an introduction to spray coating, three article digests from Wiley Online Library and the latest news about Evident's Image of the Year Award 2022.

Wiley in collaboration with Evident, are committed to bridging the gap between fundamental research and industrial applications in the field of optical metrology. We strive to do this by collecting and organizing existing information, making it more accessible and useful for researchers and practitioners alike.

EVIDENT
OLYMPUS

WILEY

A Tunable Polarization Field for Enhanced Performance of Flexible BaTiO₃@TiO₂ Nanofiber Photodetector by Suppressing Dark Current to pA Level

Li Su, Tingting Yan, Xinya Liu, Fa Cao, and Xiaosheng Fang*

The flexible titanium dioxide (TiO₂) nanofibers (NFs) film are promising candidates for high-performance wearable optoelectronic devices. However, the TiO₂ ultraviolet photodetectors (UV PDs) generally suffer from low photosensitivity, which limits the practical applications. Herein, a TiO₂ (TO) NFs film flexible photodetector integrated by ferroelectric BaTiO₃ (BTO) NFs is developed via electrospinning technology with double sprinklers and in situ heat treatment. Compared with TO NFs PD with poor on/off ratio ≈ 44 , the BTO@TO NFs PD-2 exhibits an excellent on/off ratio of $\approx 1.5 \times 10^4$ due to the dramatically restrained dark current. The ultralow dark current (pA level) is attributed to the depletion of photogenerated carriers by the space high-resistance state induced by the downward self-polarization field in ferroelectric BaTiO₃ NFs. The ferroelectric domain with larger downward orientation in polarized BTO@TO NFs exhibits stronger self-polarization field to modify the directional transport of photogenerated carriers and enhances the band bending level, which improves the photocurrent of device. The special structure woven by ferroelectric nanofiber with self-polarization will provide a promising approach for improving the performance of flexible photodetectors.

1. Introduction


The flexible photodetectors can be integrated into portable and wearable devices for next-generation optoelectronic devices.^[1–3] Hence, an appropriate semiconductor with high photoelectric performance and excellent mechanical flexibility is highly desired for the construction of wearable UV irradiation monitoring systems.^[4–6] Owing to the advantages of excellent chemical stability and photoelectric characteristic, the TiO₂ is one of the most competitive sensitive material candidates for the construction of UV photodetector. Now, the researches of

TiO₂-based flexible photodetector mainly focus on it integrate on soft substrates such as plastic or polymers. The device faces challenges of materials compatibility, processing techniques, and also inevitably invalidation due to breakage during bending.^[7–9] In contrast, 1D inorganic semiconductor nanofibers prepared via electrospinning and appropriate modification have excellent mechanical flexibility for many applications such as solar cells, sensors, and so on.^[10–14] For example, a highly mechanically flexible UV PD consisting of Y³⁺-doped TiO₂ nanofiber film was prepared. It can bear continuous bending for >2000 times and the photocurrent remains $\approx 60\%$ of its initial level.^[15] Although the mechanical flexibility of TiO₂ nanofiber via doping has been optimized, the poor photodetection performance of it has not been improved. Especially, intrinsic defects in electrospun nanofiber results in high dark current, which leads to a low on/off ratio, limiting the practical applications. How to reduce

the dark current to improve the on/off ratio and optimize the sensitivity of the device is still a research concern. The current research mainly through the design of heterojunction, PN heterojunction, gate and other strategies to achieve the purpose of reducing dark current. A typical study of PN heterojunction reports that the on/off ratio of nanotube TiO₂-BiOCl was up to $\approx 10^5$ owing to low dark current.^[16] But, this heterojunction structures still suffer from the problems such as instability of physical structure and uncontrollable morphology, which is hindered of them in widespread use. The traditional film-based phototransistor applies gate voltage to forms depletion region, which induces the effective suppression of dark current, thus improves on/off ratio of the device.^[17,18] However, the introduction of the gate makes the device structure design complex and increases the power consumption. Hence, it makes sense to explore new strategy for high performance flexible photodetector composed of TiO₂ nanofiber.

At present, the ferroelectric material with permanent electrical polarization induced by ionic displacement has shown great promises in engineering the interfacial band structure and controlling the charge transfer properties of heterojunction.^[19] As a consequence, the internal carrier concentration in the semiconductor can be effectively tuned toward favorable

L. Su, T. Yan, X. Liu, F. Cao, X. Fang
Department of Materials Science
Institute of Optoelectronics
State Key Laboratory of Molecular Engineering of Polymers
Fudan University
Shanghai 200433, P. R. China
E-mail: xshfang@fudan.edu.cn
L. Su, F. Cao
Zhangjiang Fudan International Innovation Center
Shanghai 201210, P. R. China

 The ORCID identification number(s) for the author(s) of this article can be found under <https://doi.org/10.1002/adfm.202214533>.

DOI: 10.1002/adfm.202214533

direction under the regulation of ferroelectric polarization filed.^[20] Introducing the ferroelectric materials to field-effect transistor enabled the self-polarization gating effect.^[21] A variety of photoelectric detection studies have evidenced the effectiveness of implementing polarization filed through ferroelectric film to replace the external electric filed produced by the gate to adjust the performance of photoelectric devices.^[22,23] Recent study reported that the BTO-ZnO UV photodetector exhibits an ultrahigh on/off ratio of $\approx 14\ 300$ and ultrafast response speed (0.11/5.80 ms) because of the spatial distribution of electron concentration of ZnO film is regulated by the self-polarization of BaTiO₃ film.^[24] Moreover, the TiO₂ composite ferroelectric materials have also been widely used in solar cells and photocatalysis and other fields.^[25,26] For instance, Wang et al. developed BaTiO₃-coated TiO₂ NWs as photoelectrochemical photoanodes, which achieved 67% photocurrent density by adjusted of the ferroelectric polarization via external electric poling.^[19] One can expect improved device performance when ferroelectric is appropriately introduced to Photoelectric detection system.

In this work, we fabricate a flexible nanofiber film photodetector (NFs PD) integrate by ferroelectric phase BaTiO₃ NFs and TiO₂ NFs via a one-step electrospinning technology with double

sprinkler and in situ annealing. The flexible photodetector constructed from BTO@TO NFs exhibits an excellent on/off ratio of $\approx 1.5 \times 10^4$ under 320 nm UV light at 2 V bias, while the pristine TO NFs PD shows a poor photoelectricity with low on/off ratio of ≈ 44 . The excellent performance is attributed to the formation of a space high-resistance state at interface induced by the self-polarization field on BaTiO₃ nanofiber, resulting in low dark current to pA level. On the other hand, a tunable polarization field via polarized of BaTiO₃ NFs increases the band bending of TiO₂ in polarized BTO@TO NFs and promotes the photogenerated carrier migration, resulting in improved photocurrent. This research provides a demonstration of the ferroelectric nanofiber in organization structure as effective strategy for improving the ultraviolet photodetectors performance.

2. Results and Discussion

By electrospinning technique, a dual nozzle device was employed to obtain the BaTiO₃ NFs and TiO₂ NFs simultaneously, and then in situ annealing treatment at 700 °C was conducted (Figure 1a). On the one hand, the amide groups of

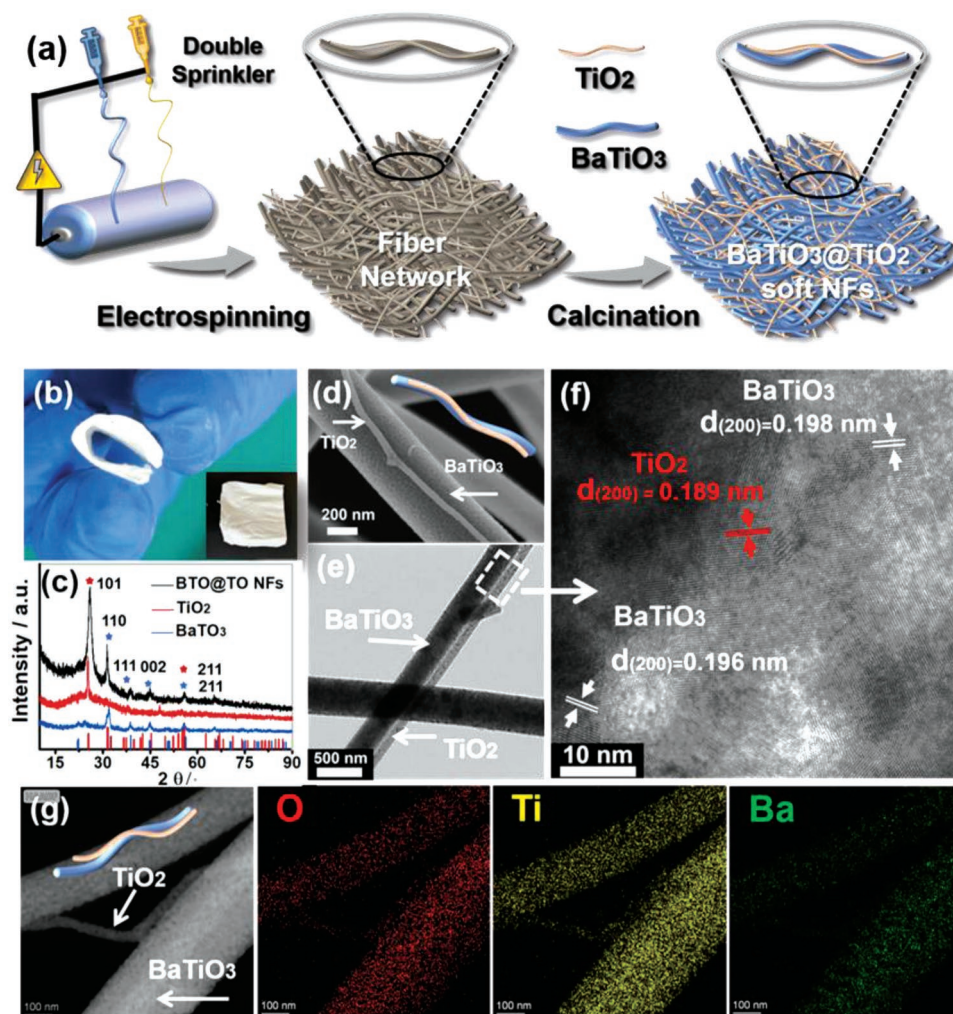


Figure 1. a) Synthesis illustration by electromechanical coupling procedure. The BTO@TO soft NFs films characterization. b) A bending optical image. c) XRD patterns, d) SEM image, e) TEM image, f) HRTEM image, and g) corresponding EDS mapping images.

Polyvinylpyrrolidone (PVP) could hydrogenate with alkoxides at the molecular scale by strong hydrogen bonding, and on the other hand, a stable sol was formed by O-bridged metal organic groups, this inhibits the condensation reactions and promoting structural relaxations.^[27] Subsequently, due to the synergy of the electrical field and capillary forces at the Tylor cone, the soft organic-inorganic fiber network was formed. The in situ heat treatment process was accompanied by the decomposition of polymer, crystal nucleation, and growth until densification, forming a flexible composite nanofiber film. In the annealing process, a certain concentration of PVP can relieve the evolve stress to a certain extent, making the structure relaxation, which facilitated the formation of crack-free composite nanofiber film consisted of BaTiO₃ NFs and TiO₂ NFs (denoted as BaTiO₃@TiO₂ nanofibers, BTO@TO NFs). The obtained BTO@TO NFs film exhibits good mechanical flexibility which could maintain its origin shape without fragility after bending (Figure 1b).

The X-ray diffraction (XRD) patterns of nanofiber films are displayed in Figure 1c. The diffraction peaks with 2θ of 25.3° and 55.1° are indexed to the (101) and (211) crystal facets of anatase phase titanium dioxide (JCPDF No. 21–1272). Due to the thinness of the titanium dioxide NFs film, a slightly bulging diffraction peak originates from the background peak of the quartz sample stage. And, the diffraction peaks emerge at 31.6°, 38.8°, 44.8°, and 56.2° which correspond to the (110), (111), (002), and (211) crystal facets of tetragonal phase barium titanate (JCPDF No. 05–0626). The characteristic diffractions of both anatase phase titanium dioxide and tetragonal phase barium titanate in BTO@TO NFs can be clearly observed, indicating no crystal phase transition of nanofiber by spinning with double sprinklers. Furtherly, the surface composition and the oxidation states of BaTiO₃ NFs and TiO₂ NFs were analyzed by the X-ray photoelectron spectroscopy (XPS). Figure S1a,d (Supporting Information) displays the survey spectrum of TiO₂ NFs and BaTiO₃ NFs, they reveal the dominant existence of element Ti, O and Ti, Ba, O. Moreover, the Ti 2p display two splitting peaks located at 464.2 and 458.2 eV which corresponds to the Ti 2p_{1/2} and Ti 2p_{3/2}, respectively (Figure S1b,e, Supporting Information). In the Figure S1f (Supporting Information), the binding energy peak emerging at 794.5 and 778.1 eV are related to Ba 3d₃ and Ba 3d₅, revealing the presence of Ba²⁺ in BaTiO₃ nanofiber. Moreover, the O 1s of TiO₂ NFs and BaTiO₃ NFs region shows two separated peaks located at 530.0 ± 0.2 and 532.5 ± 0.2 eV, respectively. The first peak is assigned to the metal oxides lattice oxygen and the second might be related to the hydroxyl groups, in agreement with the previous literature (Figure S1c,g, Supporting Information).^[16] By the field emission scanning electron microscope (FESEM), the microstructure of NFs films further was checked. The SEM images show that the BaTiO₃ NFs and TiO₂ NFs were composed of continuous and uniform nanofiber with diameters ≈500 and ≈150 nm, respectively (Figure S2a,b, Supporting Information). For the BTO@TO NFs, SEM image displays a homogeneously cross-aligned in a 3D mesh format composed both the BaTiO₃ NFs and TiO₂ NFs with dense and smooth surfaces, which are favorable microstructure for achieving high mechanical flexibility properties (Figure 1d; Figure S2c,d, Supporting Information).^[15] The transmission electron microscope (TEM) of BTO@TO NFs displays a smooth interface formed by a BaTiO₃ NFs and TiO₂ NFs

(Figure 1e). The diameters of the BaTiO₃ NFs and TiO₂ NFs are about ≈460 and ≈160 nm, which are consistent with the above SEM results. The interface was partially magnified to further observe the lattice structure. The high-resolution transmission electron microscope (HRTEM) image demonstrates that BTO@TO NFs had clear lattice fringes with lattice spacing of 0.196 nm, which are ascribed to the (200) plane of tetragonal phase barium titanate, and the lattice spacing of 0.189 nm is ascribed to the (200) plane of anatase phase titanium dioxide (Figure 1f). Moreover, the TEM and corresponding EDS mapping images show that the element of Ti, Ba, and O were evenly distributed in coarse nanofiber, however, the finer nanofiber exhibited stronger signals of Ti and O elements, and the signal of Ba element is hardly detected (Figure 1g; Figure S2e, Supporting Information). It indicates that the fiber with larger diameter corresponds to barium titanate, while the finer one fiber is attributed to titanium dioxide.

The photoelectric properties of the pristine TiO₂ NFs and BTO@TO NFs were investigated in ambient by using a two-probe method with silver pastes as the electrodes (denoted as TO NFs PD and BTO@TO NFs PD). Figure 2a presents a typical current-voltage (*I*–*V*) curve of the TO NFs PD and BTO@TO NFs PD in the dark and 320 nm light illumination. For the TO NFs PD, the response current increases from dark current of 1.0 × 10^{–10} A to a photocurrent of 3.7 × 10^{–8} A, resulting in an initial on/off ratio of ≈370. Moreover, the pure BTO NFs PD has no obvious photo-response at the same condition (Figure S3, Supporting Information). Compared with the TO NFs PD, when the was interwoven with TiO₂ NFs to form BTO@TO composite nanofiber fil BaTiO₃ NFs m, the dark is current significantly reduced to 2.7 × 10^{–12} A, while the corresponding photocurrent was 6.1 × 10^{–9} A. Although the photocurrent of BTO@TO NFs PD is slightly lower than that of TO NFs PD, the dark current is significantly lower than that of TO NFs PD, resulting in a higher initial on/off ratio of ≈2.2 × 10³. Low dark current might be caused by the depletion layer formed by the self-polarization of BaTiO₃ NFs.^[24,28] Further, the current-time transient response (*I*–*t*) characteristics were measured under 320 nm at 2 V bias (Figure 2b). The results show that both TO NFs PD and BTO@TO NFs PD exhibit stable photocurrents with the light on-off switching. And, the photocurrent of TO NFs PD decays slowly from 8 × 10^{–9} A to 2.2 × 10^{–10} A, while the BTO@TO NFs PD shows a fast and stable photo-response, which decays rapidly from 5.5 × 10^{–9} A to 2.6 × 10^{–12} A. For the TO NFs PD, the latent crystal defect and a slow adsorption of oxygen molecules on the TiO₂ nanofiber may be potential cause for the poor photoelectric properties.^[16] More importantly, this improvement of BTO@TO NFs PD is mostly associated with the remarkable suppressed dark current caused by the introduction of ferroelectric phase BaTiO₃ NFs in the composite NFs film. Hence, the piezoelectric response force microscopy (PFM) with dual alternative current mode was used to characterize the ferroelectricity of BTO@TO NFs. In Figure S4a (Supporting Information), the height sensor image displays a distance of 59.8 nm from the highest point to the lowest point (the color contrast indication height). Figure S4b (Supporting Information) is the corresponding amplitude image in the vertical piezoelectric response. The amplitude value represents the magnitude of amplitude, and the phase represents the angle

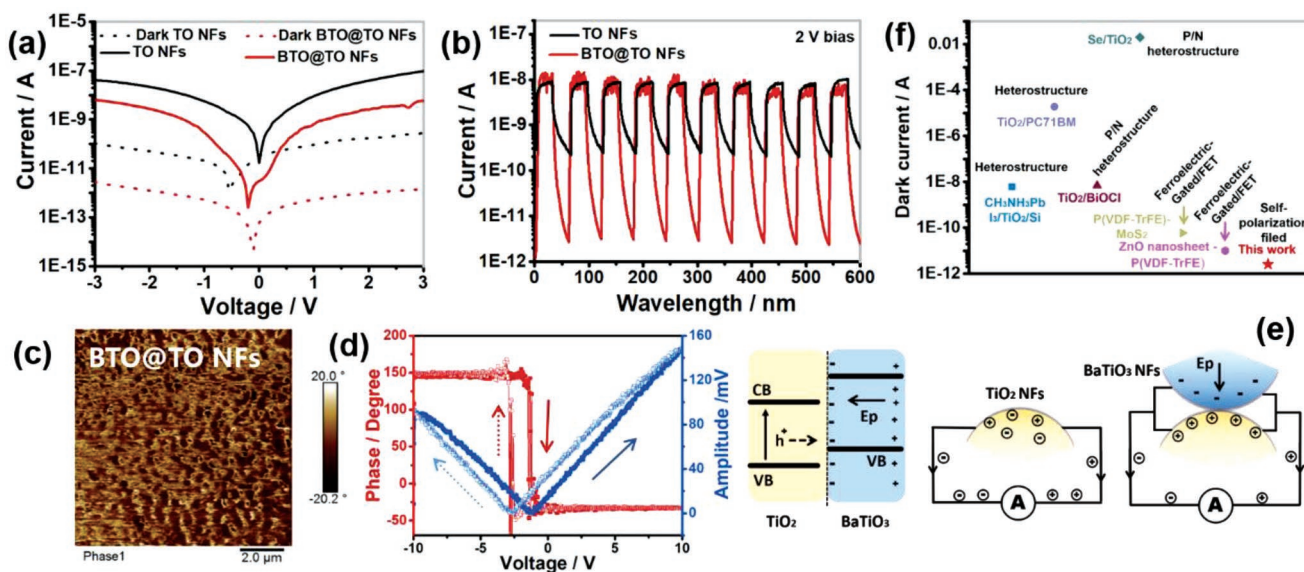


Figure 2. Comparison of photoelectric performance between TO NFs PD and BTO@TO NFs PD. a) I - V characteristics and b) I - t characteristics under dark and 320 nm light. BTO@TO NFs PD of c) PFM phase image and d) single point hysteresis loop obtained by PFM method (the red line represents phase change and the blue line represents amplitude change). e) Simplified schematic diagrams of the electric field in the BTO@TO NFs PD for controlling photogenerated carrier. f) Dark current level value of photodetectors based on various regulation strategy (the data from the Table S1, Supporting Information).

of the amplitude. According to the PFM principle, the same color in the phase image represents the same angle, and the orientations of the amplitudes in this region are consistent. These small regions with consistent orientations were denoted ferroelectric domain. Among them, the light-colored regions indicate the upward polarization direction of domain, whereas dark-colored regions indicate downward polarization direction of domain.^[29,30] For the phase image of BTO@TO NFs, the phase angle was changed nearly 180°. It indicates that there are two kinds of antiparallel domains in the selected region, which have a self-polarization (Figure 2c). Subsequently, the PFM test was carried out on a certain region of BTO@TO NFs to obtain the function between amplitude (and phase) of piezoelectric response and the direct bias voltage variation of a scanning probe tip. As Figure 2d shows, the curves obtained by forward scanning (from -10 to +10 V) and reverse scanning (from +10 to -10 V) do not return, showing a typical hysteresis curve, which proves a good ferroelectricity of BTO@TO NFs. Moreover, the amplitude of the probe at +10 V bias is higher than that at -10 V bias, indicating that the ferroelectric domains in the test region tend to undergo downward self-polarization. As a result, a self-polarization field with a downward direction is generally formed.^[24] In BTO@TO NFs PD, the TiO₂ NFs is subjected to the downward self-polarization of the BaTiO₃ NFs. To satisfy the electrostatic equilibrium, the electrons of TiO₂ gather at the interface to form an electric field, expressing as a space high-resistance state. It becomes a barrier for electrons, which deplete the electrons and holes at the interface in dark. Further, the self-polarization field induced by ferroelectric domain enhances built-in electric field at heterointerface, resulting in an ultralow dark current (Figure 2e). In Figure 2f, we summarize the dark current level of photodetectors based on various regulation strategy and our NFs photodetectors enhanced by

the self-polarization field. Our device clearly shows advantages compared to previously studies.^[16,22,31-34]

Subsequently, the current response behavior of BTO@TO NFs PD was further studied under different incident light. The I - V curve shows that the PD exhibits a good photoresponse to UV light from 280 to 400 nm. (Figure S5a, Supporting Information). The influence of light power density of BTO@TO NFs PD has also been investigated under 320 nm illumination. The concentration of photo-generated carries is positively correlated to be the absorbed photon flux.^[35] As Figure S5b (Supporting Information) shows, current-time curve with the BTO@TO NFs PD under illumination light on-off with different power densities was conducted. Based on this scenario, the photocurrent (I_{ph}) is usually described as a function of photo density according to the power law:

$$I_{ph} = \alpha p^\theta \quad (1)$$

where α is a constant under certain wavelength and the exponent θ determines the response of photocurrent to light intensity. The exponent θ of BTO@TO NFs PD was fitted to be 0.912 (Figure S5c, Supporting Information). This fractional power dependent is considered to be related to the complex behaviors of electron-hole generation, recombination and trapping effects for BTO@TO NFs PD.^[36] The responsivity was further calculated according to the following equation to reveal the spectral response of BTO@TO NFs PD:

$$R_\lambda = \frac{I_{ph} - I_d}{P_\lambda S} \quad (2)$$

where I_d is the dark current, P_λ is power density of the incident illumination, and S is the effective area under irradiation, and λ is the excitation wavelength. Moreover, the responsivity of the BTO@TO NFs PD first increases and then decreases

with the increase from 250 to 420 nm at 1 V bias (Figure S5d, Supporting Information). Compared to TO NFs PD, the responsivity of BTO@TO NFs PD is improved owing to the suppressed dark current, and the highest R value is $25.6 \mu\text{AW}^{-1}$ at the wavelength of 330 nm. In addition, the other important merit to evaluate a PD is detectivity (D^* , typically quoted in Jones), which reflects the ability to detect weak signals from the noise environment.^[37] Considering the shot noise from the dark current is the major contributor of background noise, the D^* can be estimated by the following formula:

$$D^* = \frac{R_\lambda}{(2eI_d|S|)^{1/2}} \quad (3)$$

where e stands for the elementary charge. Corresponding to the enhanced responsivity, the detectivity of BTO@TO NFs PD reaches to 2.75×10^7 Jones under the 330 nm wavelength.

Although the dark current of the BTO@TO NFs PD is significantly reduced under the control of the self-polarization field, the photocurrent is not improved. Recently, the localized field enhancement methods such as the ferroelectric field to enhance the photoelectric performance of photodetectors have been reported.^[38] The ferroelectrics were introduced to photodetectors owing to the polarization field, which can be used to improve the photodetection performance. For example, the study of a 2D materials/ferroelectrics hybrid system proved that

a polarization field of ferroelectric layer effectively modulated the photocurrent in a transistor. The downward polarization field induced a stronger band bending and generated a stronger built-in electric field to improve the photocurrent.^[39] The ferroelectric domains in the BaTiO₃ nanofibers are randomly oriented, leading to a weak self-polarization. Hence, we put the prepared BTO@TO NFs film in a high-voltage electric field ($\Delta\phi_1 = 10$ KV, $\Delta\phi_2 = 15$ KV) for polarization treatment, which orients the internal ferroelectric domains, thereby enhancing the remnant polarization of BaTiO₃ and promoting the photocurrent of device. (Figure 3a; Figure S6 Supporting Information). The poled NFs films are denoted as BTO@TO NFs-1 and BTO@TO NFs-2, respectively. The subsequent PFM result of BTO@TO NFs-1 show that the phase angle was changed nearly 180° (Figure 3b). Moreover, the dark-colored regions are obviously more than the light-colored regions, indicating that the ferroelectric domain is more inclined to the downward polarization. The function curves between amplitude (and phase) and voltage show a “butterfly curve” and a typical hysteresis curve, which is similar to the result of original BTO@TO NFs (Figure 3d). It indicates that this polarization conditions would not change the intrinsic ferroelectric properties of BaTiO₃. Figure S7a,b (Supporting Information) displays the corresponding height sensor image and the amplitude image. Noteworthy, the values of phase angles of BTO@TO NFs-2 are

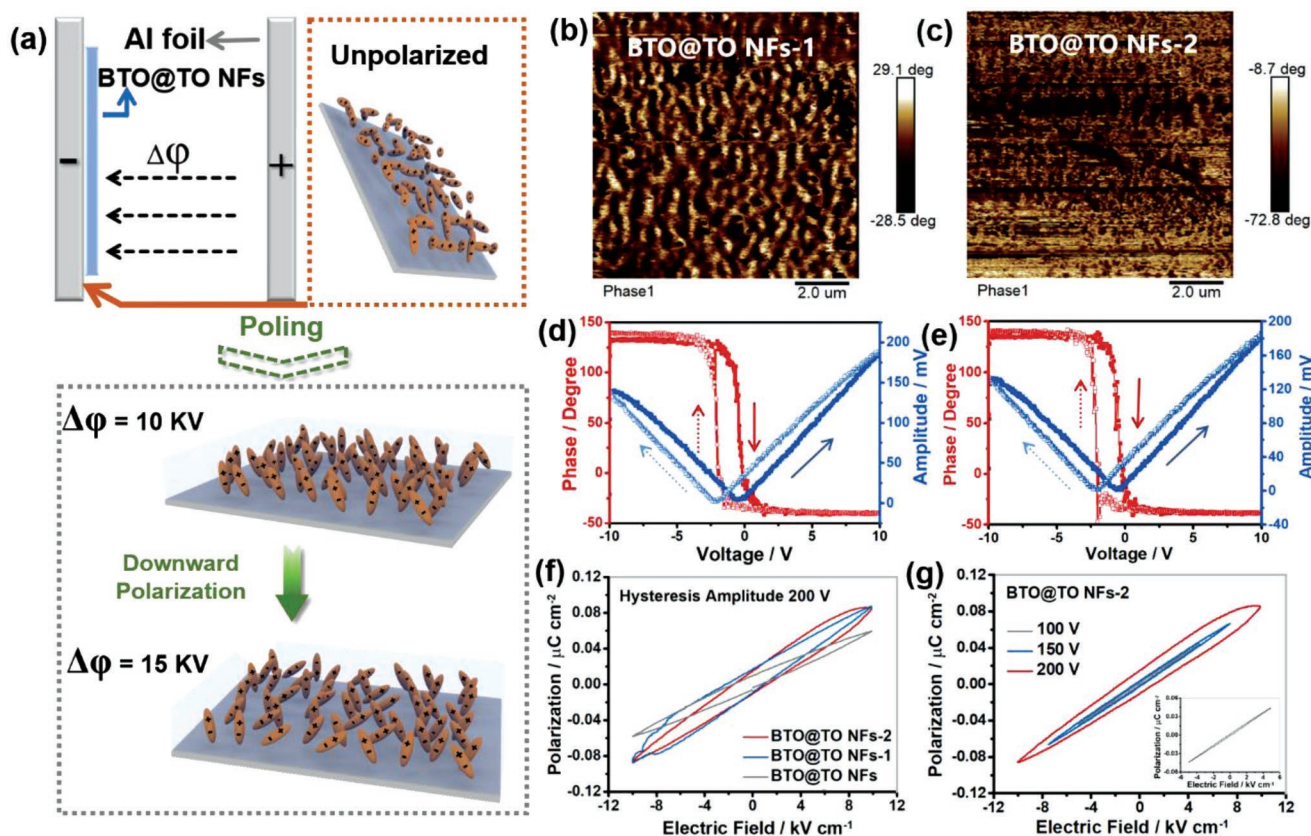


Figure 3. a) Schematic illustration of the poling process of the BTO@TO NFs film and the ferroelectric domain is gradually polarized downward with the increase of the electric field. PFM phase image and corresponding single point hysteresis loop b,d) BTO@TO NFs-1, c,e) BTO@TO NFs-2. f) Polarization–electric field loops of PE-poled BTO@TO NFs films. g) Polarization–electric field loops of PE-poled BTO@TO NFs-2 film at different hysteresis amplitude, the inset image is PE loop of sample at 100 V.

all negative in phase image (Figure 3c). Figure 3e shows that the phase angle reverses with the change of voltage, and the corresponding amplitude still shows a typical “butterfly curve”. And, the amplitude value at + 10 V bias is greater than that at - 10 V bias. The results indicate that the internal ferroelectric domains are ordered downward, and the degree of orientation is stronger.^[40,41] Figure S7c,d (Supporting Information) shows the height sensor image and the corresponding amplitude of BTO@TO NFs-2.

The ferroelectric behavior of three NFs films was further characterized by ferroelectric analyzer. In Figure 3f, although remnant polarization (Pr) turned out to be weak, the slim closed Polarization-Electric field hysteresis loops (PE loops) of three BTO@TO NFs films were clearly observed. Compared with the initial BTO@TO NFs, the Pr values of BTO@TO NFs-1 and BTO@TO NFs-2 were significantly enhanced. It indicates that the internal ferroelectricity domains tend to be oriented. Moreover, the corresponding coercive field (Ec) values of BTO@TO NFs, BTO@TO NFs-1, and BTO@TO NFs-2 is also slightly enhanced. The increase of the electric field strength will affect the switching of the surrounding domains.^[40] Combined with the PFM results, it shows that the ferroelectric domains tend to

be oriented and the polarization direction tend to be downward, which results in the enhancement of downward self-polarization. Moreover, the PE hysteresis loops of BTO@TO NFs-2 in different test electric fields show that the Pr and Ec increase with the enhanced electric field strength (Figure 3g).

Subsequently, the comparison of photoelectric properties between BTO@TO NFs PD and the polarized BTO@TO NFs PD was further investigated. The Figure 4a shows the *I*-*V* curves of these PDs in a logarithmic plot under 320 nm light illumination and in dark. The photocurrent of BTO@TO NFs-1 PD is 3.2×10^{-8} A, the same level as the TO NFs PD. Moreover, it also remains a low dark current of 6.2×10^{-12} A at ± 3 V. Meanwhile, the photocurrent of BTO@TO NFs-2 PD is increased to 2.0×10^{-7} A, which is higher than BTO@TO NFs-1 PD. It may be attributed to the modulation of the carrier distribution at the interface by the downward polarization field, resulting the improving of photocurrent. The reproducibility of photo-response is another important parameter for high performance PD. The *I*-*t* characteristics on a semilogarithmic plot of two polarized BTO@TO NFs PDs show excellent reproducibility without noticeable photocurrent decay upon 320 nm irradiation at 2 V bias (Figure 4b). And, the photocurrent of the

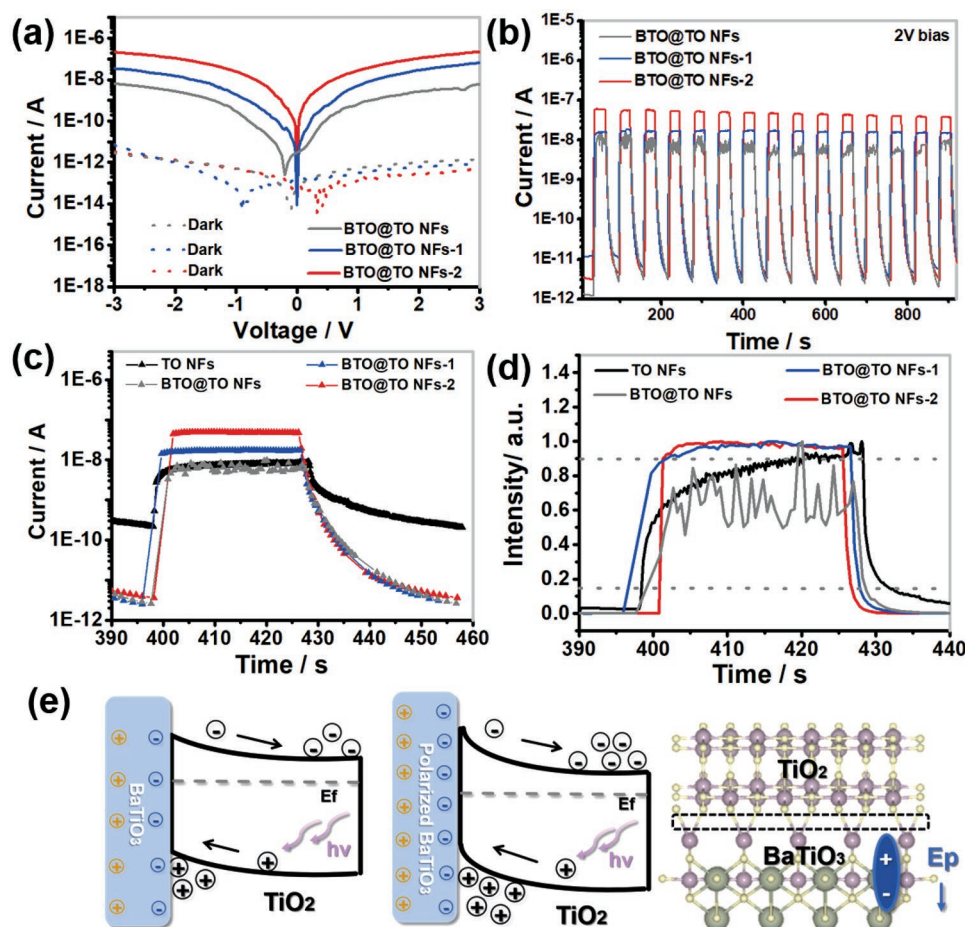


Figure 4. a) *I*-*V* characteristics, b) *I*-*t* characteristics of BTO@TO NFs PD, BTO@TO NFs-1 PD, and BTO@TO NFs-2 PD. c) single period of the *I*-*t* curve and d) the corresponding normalized *I*-*t* curves of NFs PDs. e) Energy level diagram of the BaTiO₃/TiO₂ interface, where the self-polarization in BaTiO₃ induced an upward band bending of TiO₂. The stronger self-polarization field facilitated the charge separation and transportation inside TiO₂. And, the simplified schematic diagrams of the electric field in the BTO@TO NFs.

polarized BTO@TO NFs PDs is significantly larger than that of the original BTO@TO NFs PDs. Moreover, the on/off ratio was further calculated based on a single period of the $I-t$ curves. For the TO NFs PD, the photocurrent decays slowly to $\approx 5 \times 10^{-10}$ in 30 s in dark, the on/off ratio only is ≈ 44 due to the higher dark current (Figure 4c). The photocurrent of the BTO@TO NFs PDs can rapidly decrease to $\approx 2 \times 10^{-12}$ A at the same condition. Owing to the dramatic decrease of dark current, the on/off of BTO@TO NFs PD was up to $\approx 2 \times 10^3$, which is 50 times than TO NFs PDs. Meanwhile, by applying high-voltage polarization to obtain enhanced photocurrent, the on/off ratio of BTO@TO NFs-1 PD and BTO@TO NFs-2 PD were increased to $\approx 6.7 \times 10^3$ and 1.5×10^4 , which is 167 times and 375 times than TO NFs PDs. Furtherly, the response time of NFs PDs was compared by the normalized time-dependent current curves in Figure 4d. The result show that the rise time of TO NFs PD exceeded 17 s and a decay time need 5 s. In comparison, the NFs PDs integrated with ferroelectric BaTiO₃ NFs have faster photo-response rise speed. Among them, the BTO@TO NFs-2 PD exhibits a minimum rise time of ≈ 0.5 s. The result indicates that the self-polarization field not only induced a built-in electric field to reduce the charge carrier injection in dark state, but also can facilitate the exciton separation and charge transport processes thus achieving a faster rising speed.^[24] Moreover, the $I-t$ curves of BTO@TO NFs-1 PD and BTO@TO NFs-2 PD illuminated at 0.1 V bias and 0 V bias show the reproducible light response (Figure S8a,b, Supporting Information). The photocurrent at 0 V bias can rapidly increase to a steady state of 4.1×10^{-12} A and 1.4×10^{-11} A, and then quickly decreases to 2.8×10^{-13} A and 1.2×10^{-13} A with light on/off switching, respectively. The two polarized BTO@TO NFs PDs show a self-powered performance. It is attributed to the heterojunction, which forms a built-in electric field to promote the separation of photogenerated carriers, was formed by TiO₂ NFs and BaTiO₃ NFs.

To examine the mechanism of bound-charge induced carrier concentration in self-polarization field of BaTiO₃, the UV-vis absorbance spectroscopy is further studied. As Figure S9a,b (Supporting Information) shows, the bandgaps of TiO₂ NFs and BaTiO₃ NFs are calculated to be 3.02 and 2.94 eV, respectively. And, the position of the valence band edges of TiO₂ and BaTiO₃ are determined to be 2.6 and 2.0 eV in the valence band XPS spectra (Figure S9c,d, Supporting Information). The Fermi energy bands of TiO₂ and BaTiO₃ are aligned at the same position when they form a heterojunction. The Figure 4e illustrates the effect of the BaTiO₃ in NFs PD using the schematic energy level diagram. By introducing BTO to establish a BaTiO₃/TiO₂ heterojunction, the built-in electric fields will be formed at BaTiO₃/TiO₂ interfaces. As a high-voltage polarization treatment was conducted on the NFs PD, the strong applied polarization will force the self-polarization field in domains oriented in the same direction and this will lead to an amplified polarized electric field (E_p). Thus, an enhanced the band bending level will emerge benefiting from the oriented downward self-polarization provided by BaTiO₃ NFs. This promote the transfer of photogenerated electrons at the conduction band from the BaTiO₃ to TiO₂, at the same time, the corresponding holes at the valence band will be transferred from the TiO₂ to BaTiO₃. Because of the ferroelectric domain with larger downward orientation in polarized BTO@TO NFs PDs, the device

exhibits stronger self-polarization field, resulting that the photogenerated carriers directionally move to nanofiber surface and they are effectively collected and utilized by the external electric field, so that the device outputs larger photocurrent. It indicates that the downward polarization field enhances the band bending level between BaTiO₃ and TiO₂ and regulates transport path of photogenerated charge, resulting in a higher photo-response.^[19,42]

Furtherly, the spectral responsivities of polarized BTO@TO NFs at 1 V bias and 2 V bias are shown in Figure 5a,b. The responsivity of BTO@TO NFs-2 PD reaches 2.79 and 3.8 mA W⁻¹ under 350 nm light, respectively. Owing to the decrease of dark current and the increase of responsivity, the detection sensitivity of device is correspondingly enhanced. The detectivity are increased to 3.7×10^{11} Jones under 350 nm at 1 V bias, while decreases to 12.8×10^{10} Jones at 2 V bias. It is caused by the accumulation of dark current. Presently, the flexible electronic devices have got rapid development. The device can still maintain excellent photoelectric performance when operates under single or repeated mechanical deformation states, which is an important parameter for evaluating flexible electronic device. Hence, we evaluated the photoelectric stability of NFs PD under different bending states and repeated mechanical deformation. The optical images and schematic diagram of the bending states are shown in Figure 5c. The photo-response behaviors of BTO@TO NFs-2NFs PD was measured with bending 180° under 320 nm illumination and dark state at 2 V bias. In order to conduct an effective cyclic bending test, the BTO@TO NFs-2NFs PD was attached on a PET substrate and the photoelectric measurements were performed after 100, 1000 and 2000 times of cyclic bending. Figure 5d displays the $I-t$ curve of photocurrents evolution with bending cycles. Although the photocurrent of device was attenuated after several bends, the photocurrent of device can maintain 3.03×10^{-9} A after bending 180 for 2000 cycles. The degradation of the photocurrent may be due to the fracture of partial nanofibers.^[15] Based on the excellent photoelectric performance of the NFs PD, an ultraviolet imaging system was constructed to explore the potential of device for image sensing. As shown in Figure 5e, a hollow template with "SH" graphics (4.5 cm × 3.5 cm) was placed between the incident light and the BTO@TO fiber-2NFs PD, which was used to collect the light signal. The template moved along the X axis and Y axis in the horizontal plane, and the collected photocurrent signals by a Keithley 4200 source meter were processed and analyzed. Subsequently, a 7×10 pixels' image under 320 nm light was obtained by transforming the output signal photocurrent in to the "gray code" (Figure S10c, Supporting Information). The "SH" graphics can be clearly observed, which exhibiting a red pattern. The improvement of the on/off ratio makes the contrast of the image better.

3. Conclusion

In summary, we develop a ferroelectric polarization-enhanced flexible UV PD based on BTO@TO NFs film, which was fabricated by one step electrospinning method with double sprinkler and in situ annealing. The BTO@TO NFs PD exhibits an excellent on/off ratio of $\approx 1.5 \times 10^4$, which is ≈ 341 times that of

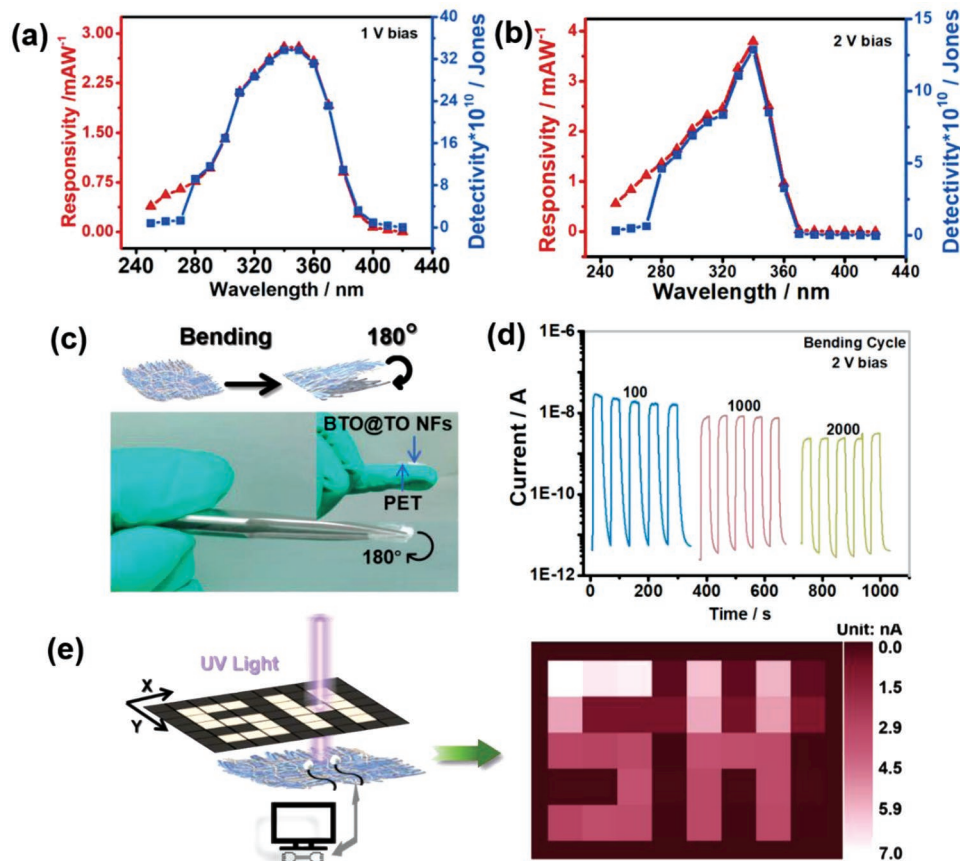


Figure 5. Photo-detecting performance of flexible BTO@TO NFs PD-2. a,b) Spectral response and detectivity at 1 V bias and 2 V bias. c) Schematic diagram and the optical image of NFs film on PET substrate, measured at 180° bending angles. d) The $I-t$ curves under 320 nm at 2 V bias, measured after a various bending cycle. e) Schematic diagram for the imaging system employing the photodetector as imaging pixel and the corresponding mapping image under 320 nm light.

the pristine TO NFs PD (on/off ratio of ≈ 44). The improvement of BTO@TO NFs PD performance was attributed to the effective suppression dark current, which was depleted of photo-generated carriers at interface via high resistivity region formed by downward self-polarization field of BaTiO₃. Moreover, the PE hysteresis loop of polarized BTO@TO NFs confirms that the strong ferroelectricity of the BTO nanofiber plays a key role of ferroelectric polarization in controlling the PD performance. This work evidences that the ferroelectric polarization field could be an effective approach to tune the performance of ultraviolet photodetectors.

4. Experimental Section

Synthesis of BTO@TO NFs Soft Film: The preparation of composite nanofiber film was performed by combining the electrospinning technique and an in situ annealing process. The spinning solution of BaTiO₃ nanofiber and TiO₂ nanofiber was prepared by slightly modifying the craft reported of previous literature.^[15,27] At first, the 7 wt.% PVP was dissolved in a mixed solution (the weight ratio of ethanol, deionized water, and acetic acid was 5:1:4, and total mass was 6 g). Subsequently, 0.9 g barium acetate was added to the above PVP solution and stirred at room temperature for 1 h. Tetrabutyl titanate was added stoichiometrically to the solution and further stirred for 2 h to form the

BaTiO₃ spinning solution. In addition, 2.94 mL tetrabutyl titanate and 0.25 wt.% yttrium nitrate hexahydrate were dissolved in a mixed solvent (the volume ratio of acetic acid to ethanol was 1:1) with vigorous stirring in an ice-water bath to form a transparent solution. And, the 8 wt.% PVP ethanol solution was added dropwise into above titanium source solution and further stirred for 30 min to form the TiO₂ spinning solution. Two spinning solution was respectively transferred into a 5 mL syringe and further were respectively arranged on two independent spray head holders. The electrospinning process was carried out with a feed rate of 1.2 mL h⁻¹, a voltage of 15 kV, and a distance between the needle tip and the substrate was 15 cm. Moreover, the relative humidity and temperature of the electrospinning chamber were kept below 35% and 26 °C. Finally, the as-spun polymeric composite nanofiber film precursors were dried at 90 °C in vacuum drying for 1.5 h and then annealed at 700 °C for 2 h at a heating rate of 1 °C min⁻¹.

BaTiO₃ nanofiber films and TiO₂ nanofiber films were also prepared according to the above steps, but only a single nozzle holder was required.

Characterization: The phase and component elements and the chemical environments analysis BaTiO₃@TiO₂ nanofiber films were studied by X-ray diffraction (XRD, Bruker D8-A25 diffractometer with Cu K α radiation ($\lambda = 1.5405 \text{ \AA}$)) and X-ray Photoelectron Spectroscopy with C 1s peak at 284.4 eV as standard signal (XPS, ThermoFisher Nexsa). The morphological and microstructures of the as-prepared BaTiO₃@TiO₂ nanofiber were characterized by the field-emission scanning electron microscopy FESEM (Zeiss Sigma) at 5 kV and HRTEM with an X-ray spectroscopy (FEI-Talos F200S and Super-x) at 200 kV. The

Temperature-dependent fluorescence spectrum at 180 K was measured by Edinburgh FLS980. The optical properties were investigated by optical diffuse absorption spectra using a UV–vis spectrophotometer (Hitachi U-4100) with an integrating sphere attachment. PFM image and local spectroscopic measurement were carried out Atomic Force Microscopy (AFM, Bruker MultiMode8, scm-pit-v2, 7000 mV Voltage Amplitude, 10 V Voltage). The hysteresis curves of polarization–electric field (P – E) were attained using a ferroelectric analyzer (TF Analyzer 2000) and the hysteresis frequency was 100 Hz.

Photoelectric Measurements: The UV PDs consisted of different NFs films were constructed by two pieces of silver pastes with fixed area and distance as electrodes. The photoelectric properties including current-voltage characteristic and the current-time transient response were conducted on a program-controlled semiconductor characterization system (Keithley 4200S, USA). A 450 W Xe lamp equipped with a monochromator was utilized as the light source, and a NOVA power meter (OPHIR photonics) was used to measure the light intensity. All these measurements were conducted under ambient conditions.

Supporting Information

Supporting Information is available from the Wiley Online Library or from the author.

Acknowledgements

The authors acknowledge financial support from the Ministry of Science and Technology of the People's Republic of China (no. 2022YFA1402904), the National Natural Science Foundation of China (No. 92263106, 62204046, and 12061131009), China Postdoctoral Science Foundation (2021M690647), the Young Scientist Project of MOE Innovation Platform, and Science and Technology Commission of Shanghai Municipality (No. 21520712600 and 19520744300).

Conflict of Interest

The authors declare no conflict of interest.

Keywords

ferroelectric domain orientation, flexible nanofiber films, polarization field, UV photodetectors

Received: December 13, 2022

Revised: January 1, 2023

Published online:

- [1] K. Nomura, H. Ohta, A. Takagi, T. Kamiya, M. Hirano, H. Hosono, *Nature* **2004**, 432, 488.
- [2] T. Sekitani, H. Nakajima, H. Maeda, T. Fukushima, T. Aida, K. Hata, T. Someya, *Nat. Mater.* **2009**, 8, 494.
- [3] T. T. Yan, Z. Q. Li, F. Cao, J. X. Chen, L. M. Wu, X. S. Fang, *Adv. Mater.* **2022**, 34, 2201303.
- [4] J. Yao, G. Yang, *Small* **2018**, 14, 1704524.
- [5] X. J. Xu, J. X. Chen, S. Cai, Z. H. Long, Y. Zhang, L. X. Su, S. S. He, C. Q. Tang, P. Liu, H. S. Peng, X. S. Fang, *Adv. Mater.* **2018**, 30, 1803165.
- [6] S. Cai, X. Xu, W. Yang, J. Chen, X. S. Fang, *Adv. Mater.* **2019**, 31, 1808138.
- [7] K. P. Bera, G. Haider, M. Usman, P. K. Roy, H.-I. Lin, Y.-M. Liao, C. R. P. Inbaraj, Y.-R. Liou, M. Kataria, K.-L. Lu, Y.-F. Chen, *Adv. Funct. Mater.* **2018**, 28, 1804802.
- [8] K. Deng, L. Li, *Adv. Mater.* **2014**, 26, 2619.

- [9] Y. H. Chen, L. X. Su, M. M. Jiang, X. S. Fang, *J. Mater. Sci. Technol.* **2022**, 105, 259.
- [10] J. Xue, T. Wu, Y. Dai, Y. Xia, *Chem. Rev.* **2019**, 119, 5298.
- [11] X. Yu, X. Wu, Y. Si, X. Wang, J. Yu, B. Ding, *Macromol. Rapid Commun.* **2019**, 40, 1800931.
- [12] Y. Zhang, S. Liu, J. Yan, X. Zhang, S. Xia, Y. Zhao, J. Yu, B. Ding, *Adv. Mater.* **2021**, 33, 2105011.
- [13] Z. H. Long, X. Xu, W. Yang, M. Hu, D. V. Shtansky, D. Golberg, X. S. Fang, *Adv. Electron. Mater.* **2020**, 6, 1901048.
- [14] S. Xia, Y. Zhao, J. Yan, J. Yu, B. Ding, *ACS Nano* **2021**, 15, 3161.
- [15] Z. Li, M. K. Joshi, J. Chen, Z. Zhang, Z. Li, X. S. Fang, *Adv. Funct. Mater.* **2020**, 30, 2005291.
- [16] W. Ouyang, F. Teng, X. S. Fang, *Adv. Funct. Mater.* **2018**, 28, 1707178.
- [17] K. E. Chang, T. J. Yoo, C. Kim, Y. J. Kim, S. K. Lee, S.-Y. Kim, S. Heo, M. G. Kwon, B. H. Lee, *Small* **2018**, 14, 1801182.
- [18] M. Naqi, M. Kaniselman, S. Choo, G. Han, S. Kang, J. Kim, Y. Yoon, S. Kim, *Adv. Electron. Mater.* **2020**, 6, 1901256.
- [19] W. Yang, Y. Yu, M. B. Starr, X. Yin, Z. Li, A. Kvit, S. Wang, P. Zhao, X. Wang, *Nano Lett.* **2015**, 15, 7574.
- [20] J. Shi, P. Zhao, X. Wang, *Adv. Mater.* **2013**, 25, 916.
- [21] J. Hoffman, X. Pan, J. W. Reiner, F. J. Walker, J. P. Han, C. H. Ahn, T. P. Ma, *Adv. Mater.* **2010**, 22, 2957.
- [22] X. Wang, P. Wang, J. Wang, W. Hu, X. Zhou, N. Guo, H. Huang, S. Sun, H. Shen, T. Lin, M. Tang, L. Liao, A. Jiang, J. Sun, X. Meng, X. Chen, W. Lu, J. Chu, *Adv. Mater.* **2015**, 27, 6575.
- [23] D. Zheng, H. Fang, P. Wang, W. Luo, F. Gong, J. C. Ho, X. Chen, W. Lu, L. Liao, J. Wang, W. Hu, *Adv. Funct. Mater.* **2016**, 26, 7690.
- [24] Y. Zhang, X. Zhao, J. Chen, S. Li, W. Yang, X. S. Fang, *Adv. Funct. Mater.* **2020**, 30, 1907650.
- [25] B. Fu, J. Li, H. Jiang, X. He, Y. Ma, J. Wang, C. Hu, *Nano Energy* **2022**, 93, 106841.
- [26] Z. Liu, L. Wang, X. Yu, J. Zhang, R. Yang, X. Zhang, Y. Ji, M. Wu, L. Deng, L. Li, Z. L. Wang, *Adv. Funct. Mater.* **2019**, 29, 1807279.
- [27] J. Yan, Y. Han, S. Xia, X. Wang, Y. Zhang, J. Yu, B. Ding, *Adv. Funct. Mater.* **2019**, 29, 1907919.
- [28] S. Chala, N. Sengouga, F. Yakuphanoglu, S. Rahmane, M. Bdirina, I. Karteri, *Energy* **2018**, 164, 871.
- [29] H. Lu, C. W. Bark, D. Esque de los Ojos, J. Alcalá, C. B. Eom, G. Catalan, A. Gruverman, *Science* **2012**, 336, 59.
- [30] A. Gruverman, D. Wu, H. Lu, Y. Wang, H. W. Jang, C. M. Folkman, M. Y. Zhuravlev, D. Felker, M. Rzechowski, C. B. Eom, E. Y. Tsymlal, *Nano Lett.* **2009**, 9, 3539.
- [31] X. Yi, Y. Wang, N. Chen, Z. Huang, Z. Ren, H. Li, T. Lin, C. Li, J. Wang, *Mater. Chem. Front.* **2018**, 2, 1847.
- [32] P. Wang, Y. Wang, L. Ye, M. Wu, R. Xie, X. Wang, X. Chen, Z. Fan, J. Wang, W. Hu, *Small* **2018**, 14, 1800492.
- [33] T. T. Yan, S. Cai, Z. Hu, Z. Li, X. S. Fang, *J. Phys. Chem. Lett.* **2021**, 12, 9912.
- [34] L. X. Zheng, K. Hu, F. Teng, X. S. Fang, *Small* **2017**, 13, 1602448.
- [35] W. Tian, T. Zhai, C. Zhang, S.-L. Li, X. Wang, F. Liu, D. Liu, X. Cai, K. Tsukagoshi, D. Golberg, Y. Bando, *Adv. Mater.* **2013**, 25, 4625.
- [36] D. Wu, Y. Jjiang, Y. Zhang, J. Li, Y. Yu, Y. Zhang, Z. Zhu, L. Wang, C. Wu, L. Luo, J. Jie, *J. Mater. Chem.* **2012**, 22, 6206.
- [37] F. P. García de Arquer, A. Armin, P. Meredith, E. H. Sargent, *Nat. Rev. Mater.* **2017**, 2, 16100.
- [38] Y. Sun, G. Niu, W. Ren, X. Meng, J. Zhao, W. Luo, Z.-G. Ye, Y.-H. Xie, *ACS Nano* **2021**, 15, 10982.
- [39] L. Tu, R. Cao, X. Wang, Y. Chen, S. Wu, F. Wang, Z. Wang, H. Shen, T. Lin, P. Zhou, X. Meng, W. Hu, Q. Liu, J. Wang, M. Liu, J. Chu, *Nat. Commun.* **2020**, 11, 101.
- [40] J. Shieh, J. E. Huber, N. A. Fleck, *J. Eur. Ceram. Soc.* **2006**, 26, 95.
- [41] T. Yim, S. H. Han, N. H. Park, M.-S. Park, J. H. Lee, J. Shin, J. W. Choi, Y. Jung, Y. N. Jo, J.-S. Yu, K. J. Kim, *Adv. Funct. Mater.* **2016**, 26, 7817.
- [42] W.-C. Tan, W.-H. Shih, Y. F. Chen, *Adv. Funct. Mater.* **2014**, 24, 6818.